High Power Laser Science and Engineering, (2023), Vol. 11, e69, 10 pages.
doi:10.1017/hpl.2023.56

HIGH POWER LASER SCIENCE AND ENGINEERING

RESEARCH ARTICLE

X-ray diffraction performance of thermally distorted crystals

Chuan Yang[1,2], Tao Liu[3], Kai Hu[1], Ye Zhu[1], Xiaohao Dong[3], Zhongmin Xu[1], Chao Feng[3], and Weiqing Zhang[1,4]

[1] *Institute of Advanced Science Facilities, Shenzhen, China*

[2] *College of Science, Southern University of Science and Technology, Shenzhen, China*

[3] *Shanghai Advanced Research Institute, Chinese Academy of Sciences, Shanghai, China*

[4] *State Key Laboratory of Molecular Reaction Dynamics, Dalian Institute of Chemical Physics, Chinese Academy of Sciences, Dalian, China*

(Received 17 April 2023; revised 11 June 2023; accepted 29 June 2023)

Abstract

The development of high-brightness X-ray free electron lasers (XFELs), such as hard X-ray self-seeding free electron lasers and XFEL oscillators (XFELOs), brings a severe challenge to the crystal monochromator due to a strong non-uniform thermal load. The distortion caused by spatial temperature gradients can severely affect the optical performance of crystals. Therefore, this paper presents a model to estimate the performance of non-uniform thermally distorted crystals. The model not only takes into account thermal strain, slope error and incident angle deviation, but also considers temperature-dependent factors such as the Debye–Waller factor and electric susceptibility. Our investigation indicates that the Debye–Waller factor reduces the height and bandwidth of rocking curves, and the impact of the electric susceptibility is tiny. The proposed model can describe the distortion of the reflectivity and transmissivity curves of non-uniform thermally loaded crystals and can be applied in the design of crystal monochromators, crystal splitters, crystal compressors and XFELOs.

Keywords: crystal monochromator; free electron laser; thermal load; X-ray diffraction

1. Introduction

X-ray free electron lasers (XFELs) are capable of producing high-brightness, ultra-short, fully coherent pulses, and provide an unparalleled tool to explore fundamental questions in chemistry, biology, atomic and molecular science, and materials science. Several hard X-ray free electron laser (FEL) user facilities are currently in operation or under construction, including LCLS[1], SACLA[2], PAL-XFEL[3], SwissFEL[4], European XFEL[5] and SHINE[6]. However, the high peak power of XFELs creates a severe thermal load on the X-ray optics, such as crystal monochromators, crystal splitters and mirrors. This thermal load issue has been a concern for several decades with the development of synchrotron radiation light sources (SRLSs) and XFELs. The optical beamline system aims to focus the beam, preserve the wavefront and purify the spectrum, but the thermal load results in wavefront disturbance, efficiency degradation and crystal lattice distortion. More generally, the thermal load is non-uniform, which brings distortion to the rocking curve, decreases the efficiency, shifts the central photon energy and broadens the bandwidth. For XFELs, the brightness is about 10 orders of magnitude higher than that of SRLSs, and the thermal load effect is severe. The high brightness brings challenges to the design of X-ray optics, such as the hard X-ray self-seeding monochromator[7], X-ray free electron laser oscillator (XFELO) cavity[8,9], crystal compressor[10] and crystal beam splitter[11,12]. The difficulties arising from a non-uniform thermal load urgently call for the investigation of X-ray diffraction by distorted crystals.

The distortion and central wavelength shift of rocking curves have attracted much attention for decades[13,14]. Researchers have realized that the central wavelength shift can be estimated by the maximum thermal strain, and the rocking curve distortion can be attributed to the slope error caused by the non-uniform thermal load. However, there is still a lack of theoretical descriptions of X-ray diffraction

Correspondence to: Chuan Yang and Weiqing Zhang, Institute of Advanced Science Facilities, Shenzhen 518107, China. Emails: yangc@mail.iasf.ac.cn (C. Yang); weiqingzhang@dicp.ac.cn (W. Zhang)

by thermally loaded crystals. Bushuev[15] developed a theoretical model to calculate the rocking curves of non-uniform thermally loaded crystals by analytically solving the equation of thermal conduction under spatiotemporal dependences of the distribution of temperature. In this model, Bushuev[16] first treated the thermal properties of the crystals as constant, and then expanded to temperature-dependent thermal properties. Bushuev applied his model to estimate the performance of the self-seeding crystal monochromator of the European XFEL. Yang *et al.*[17] investigated the transient thermal stress wave and vibration to describe the thermomechanical issues for thin diamond crystals under high-repetition-rate operation of an XFEL, but no further analysis was carried out about the distortion of the rocking curve induced by the non-uniform thermal load. Based on Bushuev's work, Qu *et al.*[18] further formulated the factors (such as the maximum strain and non-uniform thermal load) that affect the central wavelength shift and the distortion of the rocking curve, and they discussed these effects separately and quantitatively by an analytical method. They applied their method to estimate the thermal load on the self-seeding monochromator[19,20]. The above theoretical methods have successfully illustrated the central wavelength shift and the distortion of rocking curves. However, these methods are developed under the assumption that the Debye–Waller factor and electric susceptibility are temperature independent.

In this study, we focus the investigation on the temperature dependence in X-ray diffraction via the Debye–Waller factor and electric susceptibility. For a thermally loaded crystal, the vibration of atoms at different temperatures contributes to the Debye–Waller factor and further affects the form factor of atoms and the structure factor of crystals. Besides, thermal expansion changes the volume of the unit cell, which results in the perturbation of the structure factor and eventually impacts the electric susceptibility. This paper is organized as follows. In Section 2, we briefly review the dynamical theory of X-ray diffraction, the electric susceptibility and the Debye–Waller factor. Then, we establish a numerical model to estimate the rocking curves of thermally loaded crystals while considering the temperature dependence of the Debye–Waller factor and electric susceptibility. We also consider the thermal strain and incident angle deviation. These factors have a combined impact on the central photon energy shift and distortion of the rocking curves. In Section 3, under the assumption of uniform thermal load, the impact of temperature dependence on the electric susceptibility and the Debye–Waller factor in X-ray diffraction is analyzed. In Section 4, we make a comparison between our method and Bushuev's approach. Finally, we apply this model to estimate the pulse-to-pulse performance of a thermally loaded diamond crystal. This work can provide guidance to the design work of crystal monochromators, crystal splitters, crystal compressors and XFELO cavities.

2. The calculation model of X-ray diffraction by thermally loaded crystals

In this section, we first briefly review the dynamical theory of X-ray diffraction[21–23]. Then, we review the electric susceptibility and Debye–Waller factor[24]. Finally, we establish a model to estimate the rocking curves of thermal load crystals by combining the Debye–Waller factor, electric susceptibility, thermal strain and slope error.

2.1. Dynamical theory of X-ray diffraction

The dynamical theory of X-ray diffraction can accurately describe X-ray diffraction from a perfect crystal[21–23]. According to this theory, the Bragg diffraction $R_{0\mathrm{H}}$ and forward Bragg diffraction R_{00} amplitudes by a perfect thin crystal can be expressed as follows:

$$R_{0\mathrm{H}} = R_1 R_2 \frac{1 - e^{-i(\aleph_1 - \aleph_2)l}}{R_2 - R_1 e^{-i(\aleph_1 - \aleph_2)l}}, \tag{1a}$$

$$R_{00} = e^{-i\aleph_1 l} \frac{R_2 - R_1}{R_2 - R_1 e^{-i(\aleph_1 - \aleph_2)l}}, \tag{1b}$$

where

$$R_j = \frac{S(\gamma_\mathrm{h})}{\sqrt{|\gamma|}} \cdot \frac{\sqrt{\chi_\mathrm{h}\chi_{\bar{h}}}}{\chi_{\bar{h}}} \left[y \pm \sqrt{y^2 + S(\gamma_\mathrm{h})} \right], \; j = 1, 2, \tag{2a}$$

$$\aleph_j = \frac{k\chi_0}{2\gamma_0} + \frac{S(\gamma_\mathrm{h})}{2\Lambda_0} \left[y \pm \sqrt{y^2 + S(\gamma_\mathrm{h})} \right], \; j = 1, 2, \tag{2b}$$

$$y = \frac{k\Lambda_0}{2\gamma_\mathrm{h}} \left(-\alpha + \alpha' \right), \Lambda_0 = \frac{\lambda\sqrt{\gamma_0 |\gamma_\mathrm{h}|}}{P\sqrt{\chi_\mathrm{h}\chi_{\bar{h}}}}, \tag{2c}$$

and

$$\alpha = 2\sin 2\theta_\mathrm{B} \left[\Delta\theta + \left(\frac{\Omega}{\omega_0} + \frac{\Delta d}{d} \right) \tan\theta_\mathrm{B} \right], \tag{3a}$$

$$\alpha' = \chi_0 (\gamma - 1), \tag{3b}$$

and the intensities of Bragg diffraction (reflectivity) and forward Bragg diffraction (transmissivity) can be written as follows:

$$I_{0\mathrm{H}} = \gamma |R_{0\mathrm{H}}|^2, \quad I_{00} = |R_{00}|^2. \tag{4}$$

Here, the parameter α is introduced to account for a small perturbation that causes a deviation from the Bragg condition. Such perturbation may stem from various sources, such as deviations in the incident angle ($\Delta\theta$), angular frequency (Ω) and lattice spacing (Δd). The parameter α' specifically characterizes the deviation from the Bragg diffraction, which

https://doi.org/10.1017/hpl.2023.56 Published online by Cambridge University Press

arises from the refraction of the crystal. Here, γ is the asymmetry ratio, and is given by the following:

$$\gamma = \frac{\gamma_{\mathrm{h}}}{\gamma_0} = \frac{\cos\Psi_{\mathrm{h}}}{\cos\Psi_0}, \tag{5a}$$

$$\Psi_0 = \eta + \theta_{\mathrm{B}} - \frac{\pi}{2}, \quad \Psi_{\mathrm{h}} = \eta - \theta_{\mathrm{B}} - \frac{\pi}{2}, \tag{5b}$$

where η is the asymmetry angle that describes the angle between the crystal surface and the parallel reflecting atomic planes and $S(\gamma_{\mathrm{h}})$ denotes the sign of γ_{h}.

2.2. Electric susceptibility and Debye–Waller factor

In a crystal, both the charge density function $\rho(\boldsymbol{r})$ and the electric susceptibility $\chi(\boldsymbol{r})$ are triply periodic functions of the space coordinates $\boldsymbol{r}$, and the electric susceptibility can be expressed as follows:

$$\chi(\boldsymbol{r}) = -\frac{r_{\mathrm{e}}\lambda^2}{\pi}\rho(\boldsymbol{r}) = \sum_{\boldsymbol{h}} \chi_{\mathrm{h}} \exp(i\boldsymbol{h}\cdot\boldsymbol{r}). \tag{6}$$

The coefficients χ_{h} of the Fourier expansion can be related to the structure factor F_{h} of the crystal, and then we have the following:

$$\chi_{\mathrm{h}} = -\frac{r_{\mathrm{e}}\lambda^2}{\pi V_{\mathrm{c}}} F_{\mathrm{h}}, \tag{7a}$$

$$F_{\mathrm{h}} = \int \rho(\boldsymbol{r}) \exp(-i\boldsymbol{h}\cdot\boldsymbol{r})\,\mathrm{d}\boldsymbol{r}. \tag{7b}$$

It is easy to have a picture that atoms are arranged in a periodic lattice in a crystal. The vibration of the atoms can be thermally excited inside a crystal. Therefore, the vibration is temperature dependent, and can result in the decrease of the intensity of the scattered wave. The structure factor of a vibratory crystal can be expressed as follows:

$$F_{\mathrm{h}} = \sum_j \left[f_j(\boldsymbol{h}) + f_j' + f_j''\right] \exp\left(-M_j\right) \exp(-i\boldsymbol{h}\cdot\boldsymbol{r}), \tag{8}$$

where $f_j(\boldsymbol{h})$ is the form factor of atom j, f' and f'' are the dispersion corrections, $\exp\left(-M_j\right)$ is the Debye–Waller factor[24] and M_j is given by the following:

$$M_j = B_{\mathrm{T}}^j \left(\frac{\sin\theta}{\lambda}\right)^2. \tag{9}$$

If the atom vibrates isotropically and only one type of atom is considered, the thermal factor B_{T} can be written as follows:

$$B_{\mathrm{T}} = \frac{6h^2}{m_{\mathrm{A}} k_{\mathrm{B}} \Theta}\left[\frac{\phi(\Theta/T)}{\Theta/T} + \frac{1}{4}\right], \tag{10a}$$

$$\phi(x) = \frac{1}{x}\int_0^x \frac{\xi}{e^{\xi}-1}\mathrm{d}\xi, \tag{10b}$$

where m_{A}, k_{B}, Θ and h are the mass of the atom, Boltzmann constant, Debye temperature and Planck constant, respectively. The detailed derivation of Equations (9) and (10) can be found in Ref. [24].

2.3. Model of X-ray diffraction by thermally loaded crystals

In this section, we establish a numerical model to estimate the X-ray diffraction performance of thermally loaded crystals. In this model, we take the Debye–Waller factor, electric susceptibility, thermal strain, incident angle deviation and slope error into consideration.

When a series of XFEL pulses are incident on a crystal, the thermal characteristics, such as the thermal conductivity, thermal expansion coefficient, specific heat capacity and Debye–Waller factor, vary at different spatial locations due to non-uniform thermal loading. To estimate the overall reflectivity and transmissivity, we employ a weighted average method similar to that utilized in Bushuev's research:

$$\bar{I}_{0\mathrm{H}} = \frac{\int\int_{-\infty}^{+\infty} I_{0\mathrm{H}}\left(\alpha,\alpha',T,x,y\right) I(x,y)\,\mathrm{d}x\mathrm{d}y}{\int\int_{-\infty}^{+\infty} I(x,y)\,\mathrm{d}x\mathrm{d}y}, \tag{11a}$$

$$\bar{I}_{00} = \frac{\int\int_{-\infty}^{+\infty} I_{00}\left(\alpha,\alpha',T,x,y\right) I(x,y)\,\mathrm{d}x\mathrm{d}y}{\int\int_{-\infty}^{+\infty} I(x,y)\,\mathrm{d}x\mathrm{d}y}, \tag{11b}$$

where $I(x,y)$ is the intensity distribution. To establish the local reflectivity $I_{0\mathrm{H}}\left(\alpha,\alpha',T,x,y\right)$ and transmissivity $I_{00}\left(\alpha,\alpha',T,x,y\right)$, we have devised a methodological framework as depicted in Figure 1. Firstly, we obtain the thermal properties of the crystal at different temperatures, including the thermal expansion coefficient, thermal conductivity and specific heat. Secondly, we calculate the temperature distribution $T(x,y,t)$ through either a theoretical model[15,16] or thermal analysis software such as COMSOL. Thirdly, we establish the distribution of the Debye–Waller factor and the lattice spacing at the given temperature $T(x,y,t)$, which also allows one to derive the slope error distribution. Then, we can calculate the local volume of the unit cell and the local atomic form factor. Afterwards, we construct the local structure factor F_{h} and the local Fourier coefficient of the electric susceptibility χ_{h}. Next, by substituting the local F_{h} and χ_{h} into Equation (1), we can derive the local reflectivity and transmissivity. Finally, we obtain the overall reflectivity $\bar{I}_{0\mathrm{H}}$ and transmissivity $\bar{I}_{00}$ by using Equation (11).

https://doi.org/10.1017/hpl.2023.56 Published online by Cambridge University Press

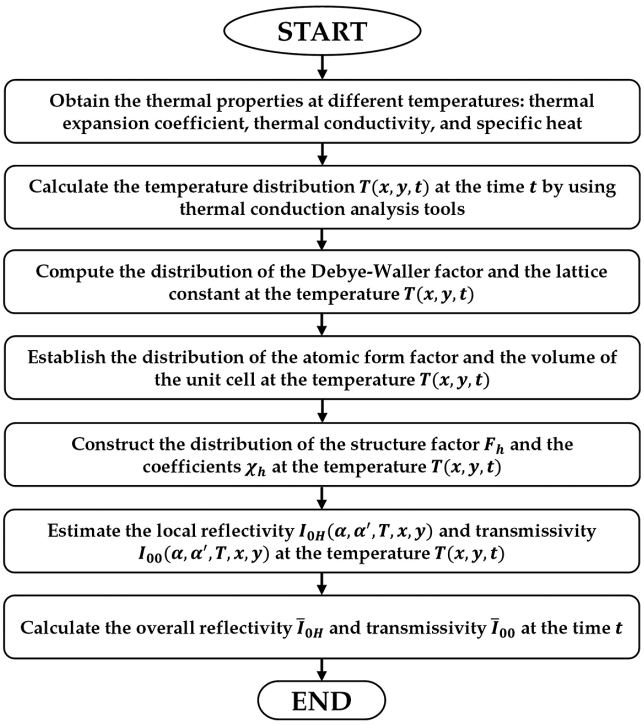

Figure 1. The calculation framework of the local reflectivity and transmissivity.

3. Temperature dependence of the electric susceptibility and Debye–Waller factor

In this section, we study the influence of the Debye–Waller factor and electric susceptibility on X-ray diffraction.

3.1. Efficiency degradation induced by the Debye–Waller factor

In this section, we discuss the impact of the Debye–Waller factor in dynamical X-ray diffraction. Figure 2 shows examples of calculations by taking the Debye–Waller factor into account in X-ray diffraction. In order to include the effect of thermal expansion, we use the data by interpolating the thermal expansion coefficient of silicon in Table 1. The specific heat capacity of a silicon crystal is fitted from Okhotin *et al.*'s work[25]. The thermal expansion coefficient is extracted and fitted from Refs. [26,27]. The thermal conductivity is fitted from Kazan *et al.*'s work[28]. The X-ray photon energy is 15 keV and the thickness of the crystal is 0.5 mm. The reflectivity curves of Si(111), Si(333), Si(555) and Si(777) are calculated at different temperatures in Figure 2(a). The rocking curves of Si(777) at temperatures of 100, 300, 500 and 700 K are shown in Figure 2(b).

It is evident that as the temperature increases, the Debye–Waller factor exhibits a decline in the height of the rocking curves and a narrowing of the bandwidth of the rocking curves. In addition, as illustrated in Figure 2(a), a more significant reduction in reflectivity is observed at higher Miller index reflections. Our findings are consistent with the study conducted by Chung[29]. Thus far, we can infer that the Debye–Waller factor plays a crucial role in X-ray diffraction. We have integrated this effect into our method of X-ray diffraction by non-uniform thermally loaded crystals.

3.2. Photon energy shift caused by electric susceptibility

According to the dynamical theory of X-ray diffraction, the central photon energy shift of the rocking curve arises from two terms, α and α'. The parameter α can describe a small perturbation that results in a deviation from the Bragg condition. The perturbation could derive from incident angle deviation $\Delta\theta$, angular frequency deviation Ω and lattice deviation Δd. The parameter α' is the deviation from the Bragg condition due to the refraction of crystals. The refractive index is temperature dependent, which is due to the electric susceptibility change with the temperature. In

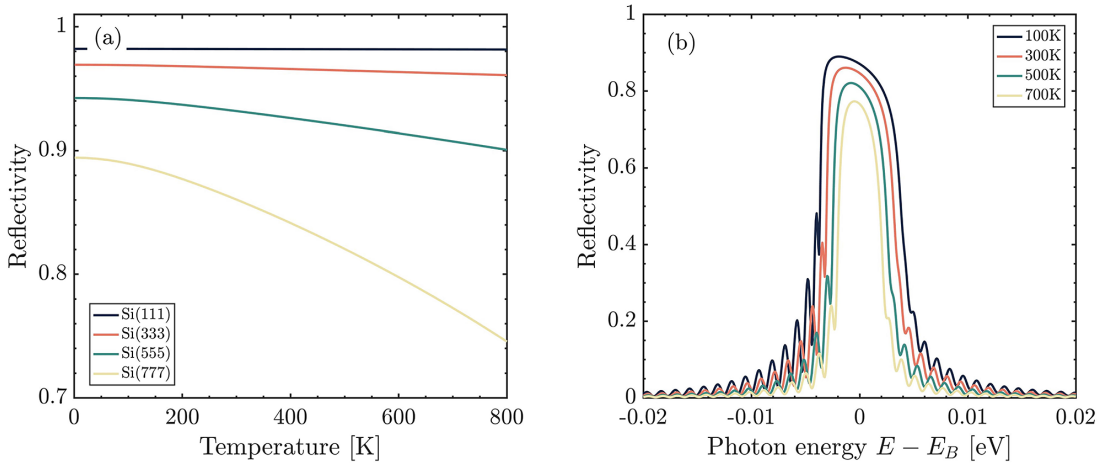

Figure 2. (a) Reflectivity as a function of temperature for Si(111), Si(333), Si(555) and Si(777). (b) Rocking curve calculations of Si(777) at different temperatures (100, 300, 500 and 700 K).

https://doi.org/10.1017/hpl.2023.56 Published online by Cambridge University Press

Table 1. Thermal properties of silicon crystal.

T [K]	α_L [10^{-6} K^{-1}]	c_p [J·kg^{-1}·K^{-1}]	κ [W·m^{-1}·K^{-1}]
50	–0.2774	118.5994	2873.6830
100	–0.3476	258.8855	967.1799
150	0.5976	370.2560	455.3698
200	1.5386	493.5994	290.8178
250	2.1829	605.0264	193.4532
300	2.6355	668.5617	148.2546
350	2.9939	719.7289	116.3444
400	3.2398	760.3916	94.9167
450	3.4382	792.8765	80.8086
500	3.6003	816.9804	69.8529
550	3.7510	835.5892	62.0598
600	3.8444	851.8373	55.0506
650	3.9265	863.8931	50.3701
700	4.0044	875.1506	46.2285
750	4.0561	882.9556	42.0751
800	4.1118	893.9759	39.6347
850	4.1626	898.3810	35.9539
900	4.1983	909.7660	33.2159
950	4.2325	918.7726	31.6155
1000	4.2748	926.0354	30.9976

this section, we investigate the temperature dependence of electric susceptibility, which may contribute to the central photon energy shift of the rocking curve.

The coefficients χ_h are related to the volume of the unit cell V_c and the structure factor F_h. There is no doubt that χ_h is temperature dependent, as V_c changes with the thermal expansion and F_h changes with the Debye–Waller factor. Electric susceptibility χ_h is associated with several physical quantities, such as the refractive index n, crystal detuning effect α', Darwin width and extinction length. The central photon energy shift caused by quantity α has been investigated in Refs. [15,16,18]. These studies show that the shift is mainly attributed to the maximum thermal strain ($\Delta d/d$). Here, we discuss the central photon energy shift arising from the quantity α'. The shift can be expressed as follows:

$$\frac{\Omega_{\text{detuning}}}{\omega_0} = \frac{\alpha'}{4\sin^2\theta_B}, \quad \alpha' = \chi_0(\gamma - 1), \tag{12}$$

where χ_0 is temperature dependent. In general, χ_0 is a very small complex parameter. The imaginary part $\mathrm{Im}(\chi_0)$ and the real part $\mathrm{Re}(\chi_0)$ are related to the cross-section of photon absorption and the atomic Thomson scattering amplitude, respectively. Typically, for diamond and silicon crystals, $\mathrm{Re}(\chi_0) \gg \mathrm{Im}(\chi_0)$, and $\mathrm{Re}(\chi_0)$ is in the range of 10^{-4}–10^{-7} for 3–25 keV.

Figure 3 illustrates the variation of the photon energy shift that corresponds to α' and the thermal strain ($\Delta d/d$) as a function of temperature. The thermal expansion data can be acquired by interpolating the data presented in Tables 1 and 2. The thermal expansion coefficient α_L and specific capacity c_p of diamond crystal are extracted from Reeber and Wang's work[30], and the thermal conductivity of diamond crystal is extracted and fitted from Wei *et al.*'s work[31]. Subsequently, the photon energy shift caused by α' at varying temperatures can be calculated by modifying the volume of the unit cell and the Debye–Waller factor. The lattice constants corresponding to different temperatures are calculated based on the thermal expansion coefficient and the lattice constant at the reference temperature. In Figure 3, the reference temperatures of diamond and silicon are respectively specified as 293.15°C and 298.15°C. The numerical method utilized in this analysis is elaborated in Figure 1. The computations presented in Figures 3(a) and 3(b) pertain to C*(400) and Si(400) at 9 keV, respectively. For a crystal with a specific Miller index and a given photon energy, the photon energy shift attributable to α' is roughly three orders of magnitude lower than the shift caused by thermal strain.

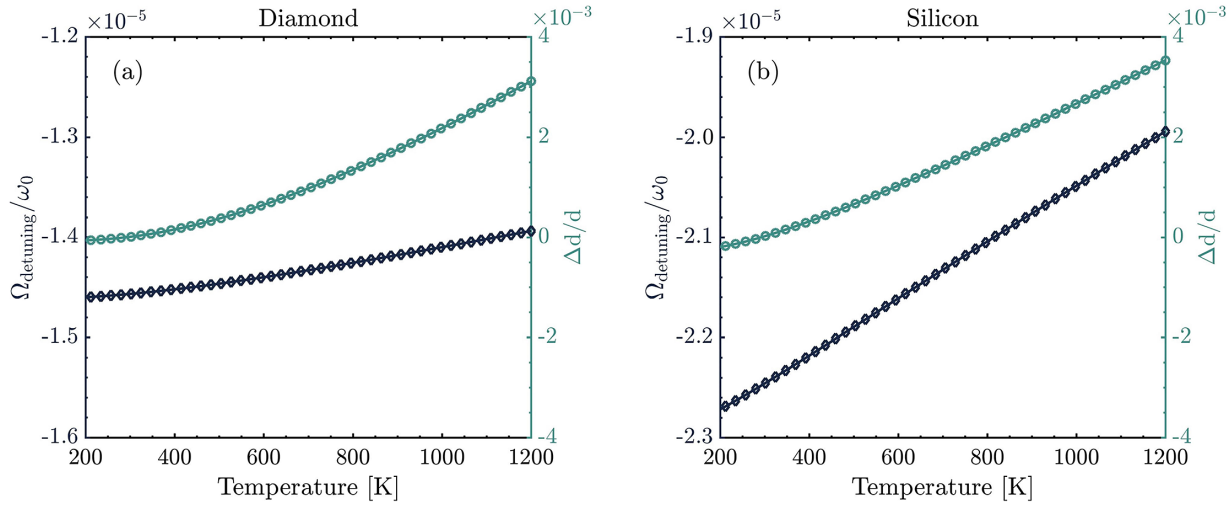

Figure 3. (a) Temperature dependence of the photon energy shift induced by α' and lattice expansion in C*(400). (b) Temperature dependence of the photon energy shift induced by α' and lattice expansion in Si(400). The calculation is performed under the assumption of a uniform thermal load.

https://doi.org/10.1017/hpl.2023.56 Published online by Cambridge University Press

Table 2. Thermal properties of diamond crystal.

T [K]	α_L [10^{-6} K^{-1}]	c_p [J·kg^{-1}·K^{-1}]	κ [W·m^{-1}·K^{-1}]
50	0.0133	4.3612	18,437.4342
100	0.0494	17.3752	11,884.3216
150	0.1897	83.3522	6798.4500
200	0.4305	198.3496	4171.0213
250	0.7105	346.2133	2930.0175
298	1.0042	506.4979	2231.2685
300	1.0169	513.3712	2214.1725
350	1.3484	684.6461	1821.5428
400	1.6953	848.0359	1601.4804
450	2.0433	996.8766	1373.5656
500	2.3798	1127.1209	1226.8272
550	2.6961	1274.9149	1076.6047
600	2.9874	1342.6712	950.1536
650	3.2521	1428.0470	858.9447
700	3.4904	1501.5253	792.8823
750	3.7037	1564.8506	734.8161
800	3.8942	1619.5581	677.0152
850	4.0640	1667.0085	628.1303
900	4.2153	1708.3531	579.3255
950	4.3504	1744.4643	537.3917
1000	4.4710	1776.1793	506.3727
1100	4.6760	1804.1610	458.4945
1200	4.8416	1870.5218	413.9395
1300	4.9768	1903.7719	374.8696
1400	5.0881	1930.8117	343.0945
1500	5.1807	1953.0017	318.3161
1600	5.2584	1971.4585	293.5377

As a result, thermal strain predominantly governs the central photon energy shift of the rocking curve, and the influence of α' can be disregarded.

4. Comparison and validation

In this section, a numerical validation of the proposed model is performed and compared with the model by Bushuev. Then, we applied the model to estimate X-ray diffraction performance in the dynamic pulse-to-pulse process.

4.1. Comparison

Here, the analytical model developed by Bushuev[15,16] is employed to compute the temperature distribution under the assumption of a 2D infinite domain:

$$T(x,y,t) = \sum_{j=1}^{n} \frac{\Delta T_j}{\sqrt{\beta_x \beta_y}} \exp\left(-\frac{x^2}{r_x^2 \beta_x} - \frac{y^2}{r_y^2 \beta_y}\right). \tag{13}$$

Here,

$$\beta_x = 1 + \frac{\sin^2\theta_B (t - t_j)}{\tau_T}, \quad \beta_y = 1 + \frac{(t - t_j)}{\tau_T}, \tag{14a}$$

$$\Delta T_j = \frac{\mu Q_p}{\pi c_p \rho r^2}, \quad \tau_T = \frac{r^2 c_p \rho}{4\kappa}, \tag{14b}$$

where μ, Q_p, c_p, ρ, r and κ are the absorption factor, pulse energy, specific heat capacity, density, transverse pulse radius and thermal conductivity, respectively. Here, n is the number of pulse impingements on the crystal and t_j is the arrival time of the jth pulse.

Our study focuses on analyzing the rocking curve of a thermally loaded Si(444) with a thickness of 50 μm. The initial temperature of the crystal is set to 300 K. We consider the pulse repetition rate is 1 MHz and the pulse energy is 200 μJ. The radius of the transverse beam profile is 800 μm. It is assumed that the bandwidth of the incident pulse is significantly wider than the width of the rocking curve. The photon energy is 10 keV, and with an absorption length of 134 μm. To conduct numerical simulations, we calculate the temperature-dependent spatial distribution of the Debye–Waller factor at $T(x,y,t)$ by implementing the method outlined in Section 2. The temperature-dependent parameters of silicon, such as the specific heat capacity, thermal conductivity and thermal expansion coefficient, are obtained by interpolating the data provided in Table 1.

When heat is deposited into the crystal, non-uniform distortion occurs, leading to changes in the overall reflectivity and transmissivity curves at different time intervals, as illustrated in Figures 4(a) and 4(b). The black curves represent diffraction by a perfect Si(444) crystal at 300 K. The solid curves were obtained using our proposed method, while the circles represent the results obtained using Bushuev's method, which does not take into account the temperature dependence of the Debye–Waller factor. Both methods reveal that the rocking curves shift and distort with heat accumulation. Compared to the dashed lines, the height of the rocking curve decreases, and the width becomes slightly narrower, which indicates the evident influence of the Debye–Waller factor. Specifically, when the heat accumulation time is 10 μs, the reflectivities of our proposed model and Bushuev's model are 40% and 48%, respectively. As the heat accumulation time increases, the differences in reflectivity and transmissivity between the two models are expected to become more significant. The numerical simulation results demonstrate that for a non-uniform thermally distorted crystal, the Debye–Waller factor plays a critical role in reducing the height and width of the rocking curves.

4.2. Dynamic pulse-to-pulse process

So far, we have developed a numerical model to describe X-ray diffraction from a thermally loaded crystal and have gained an understanding of the distortion of its rocking curve. To facilitate a more intuitive understanding of the properties of a thermally loaded crystal, we investigate the case of dynamic pulse-to-pulse thermal conduction processes in this section. Specifically, we investigate C*(400) with an initial temperature of 200 K and a thickness of

https://doi.org/10.1017/hpl.2023.56 Published online by Cambridge University Press

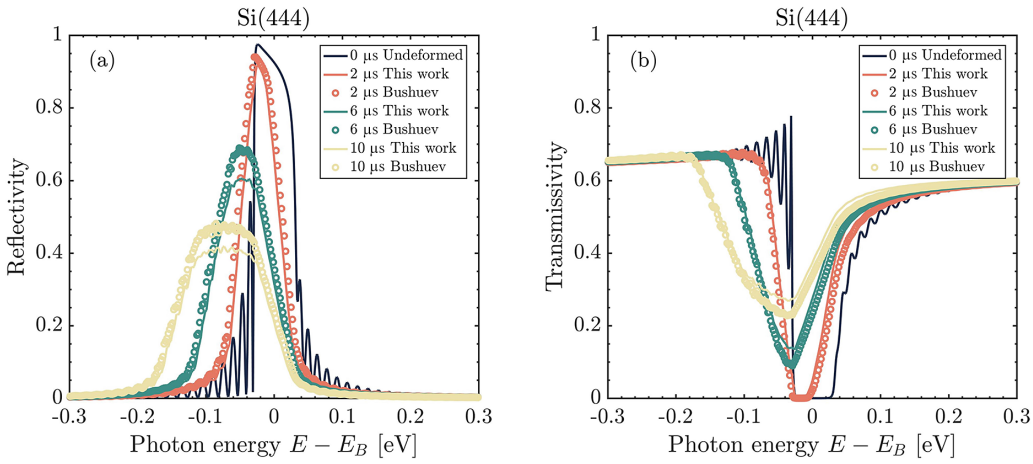

Figure 4. Comparative analysis of results obtained at 2, 6 and 10 μs using Bushuev's method (circles) and our proposed method (solid lines). The black curve refers to the undeformed crystal at 300 K.

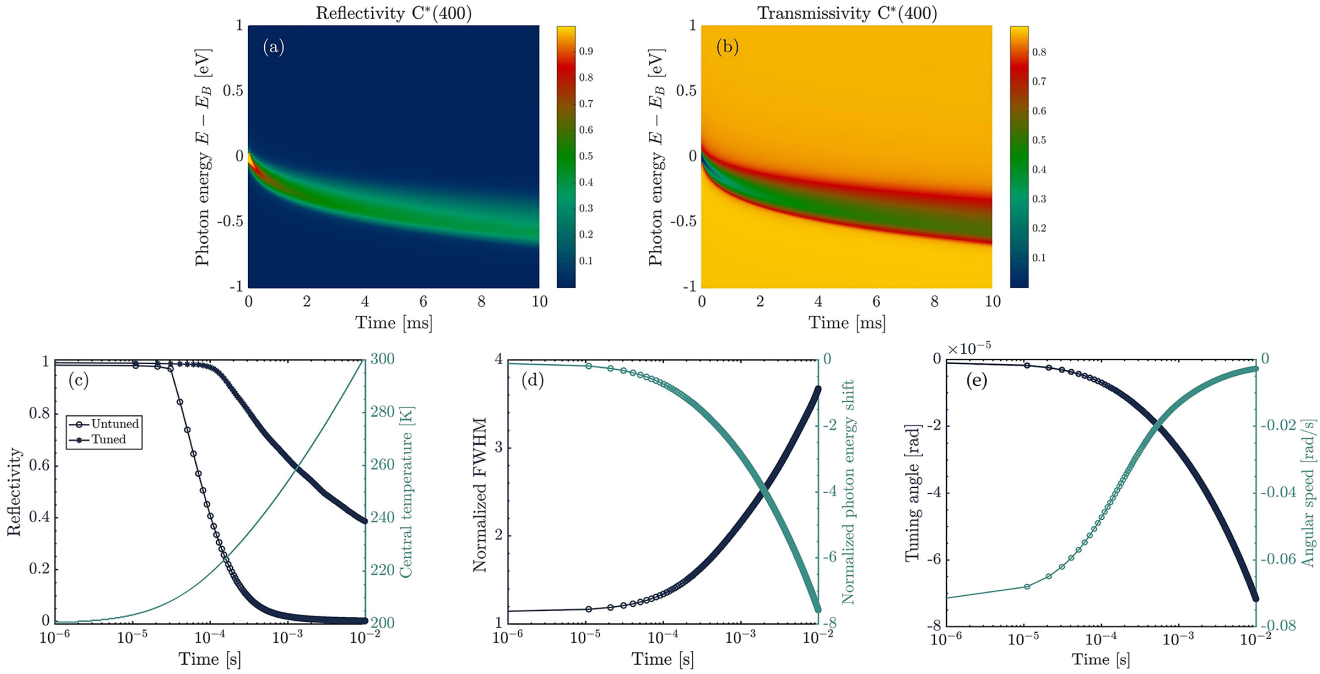

Figure 5. (a) Time evolution of the reflectivity of C*(400). (b) Time evolution of the transmissivity of C*(400). (c) Time evolution of the temperature at the crystal's center (green curve). The reflectivity curves for untuned and tuned cases are represented by circles and stars, respectively. (d) Time evolution of the normalized bandwidth and photon energy shift. The data have been normalized based on the rocking curve bandwidth (0.78 eV) of C*(400) at 200 K. (e) Time evolution of the tuning angle and the angular speed.

110 μm. The input pulse energy, repetition rate, photon energy and transverse beam radius are set at 500 μJ, 1 MHz, 9 keV and 800 μm, respectively. The absorption length is 977 μm. The temperature distribution of a diamond crystal is estimated using Equation (13). The specific heat capacity, thermal conductivity and thermal expansion coefficient of diamond can be obtained by interpolating the data in Table 2.

In the simulation, the pulse interval is 1 μs and the thermal runaway characteristic time τ_T (thermal exchange time) corresponding to the crystal at 200 K is 42.3 μs. Therefore, under these conditions, the temperature of the crystal will continue to accumulate, and the performance of the crystal will become increasingly worse. Figures 5(a) and 5(b) present the reflectivity and transmissivity records of C*(400). The results indicate a notable widening of the bandwidth and a shift in the central photon energy over time. Moreover, a decrease in reflection efficiency is observed as a result of heat accumulation. The temperature evolution at the center of the crystal is depicted in Figure 5(c), indicating a rapid temperature increase. Apparently, for this case, there is not enough time for the crystal to cool down due to the high repetition rate. Consequently, the reflectivity decreases rapidly due to distortion and the shift of the rocking curve for a fixed diffraction geometry. To optimize the reflectivity,

https://doi.org/10.1017/hpl.2023.56 Published online by Cambridge University Press

a strategy of tuning the pitch angle of the crystal can be employed, as shown in Figure 5(c) for both tuned and untuned reflectivity curves. This strategy is implemented by controlling the proper angular speed of the motor to mitigate the shift of the central photon energy, as shown in Figure 5(e), and Qu *et al.*[20] reported the strategy in their work. Furthermore, Figure 5(d) exhibits that the bandwidth and central photon energy shift increase with heat accumulation, where the latter can be compensated for by the tuning strategy, while the former can be reduced by decreasing the slope error.

5. Summary

This study investigates X-ray diffraction by a crystal under thermal load and develops a comprehensive model that not only considers several key factors, including thermal strain, incident angle deviation and slope error, but also includes the temperature dependence of the Debye–Waller factor and electric susceptibility. Our findings suggest that the influence of the Debye–Waller factor on efficiency degradation cannot be neglected, particularly in the case of high-order Miller index reflections at high temperatures. Although the Debye–Waller factor can potentially narrow the bandwidth of the rocking curve, the non-uniform thermal load still dominates the bandwidth broadening. The central photon energy shift is primarily attributed to thermal strain and slope error, while the shift induced by the temperature dependence of electric susceptibility can be neglected. The non-uniform thermal load causes variations in the local Debye–Waller factor, thermal strain and slope error, which further results in the distortion and degradation of the rocking curve. Proper cooling strategies, minimizing slope error and tuning the incident angle can effectively mitigate the effects of the thermal load.

Acknowledgements

This research was funded by the National Natural Science Foundation of China (Grant No. 12005135 and 22288201), the National Key R&D Program of China (Grant No. 2018YFE0203000) and the Scientific Instrument Developing Project of the Chinese Academy of Sciences (Grant No. GJJSTD20190002).

References

1. P. Emma, R. Akre, J. Arthur, R. Bionta, C. Bostedt, J. Bozek, A. Brachmann, P. Bucksbaum, R. Coffee, F. J. Decker, Y. Ding, D. Dowell, S. Edstrom, A. Fisher, J. Frisch, S. Gilevich, J. Hastings, G. Hays, Ph. Hering, Z. Huang, R. Iverson, H. Loos, M. Messerschmidt, A. Miahnahri, S. Moeller, H. D. Nuhn, G. Pile, D. Ratner, J. Rzepiela, D. Schultz, T. Smith, P. Stefan, H. Tompkins, J. Turner, J. Welch, W. White, J. Wu, G. Yocky, and J. Galayda, Nat. Photonics **4**, 641 (2010).
2. T. Ishikawa, H. Aoyagi, T. Asaka, Y. Asano, N. Azumi, T. Bizen, H. Ego, K. Fukami, T. Fukui, Y. Furukawa, S. Goto, H. Hanaki, T. Hara, T. Hasegawa, T. Hatsui, A. Higashiya, T. Hirono, N. Hosoda, M. Ishii, T. Inagaki, Y. Inubushi, T. Itoga, Y. Joti, M. Kago, T. Kameshima, H. Kimura, Y. Kirihara, A. Kiyomichi, T. Kobayashi, C. Kondo, T. Kudo, H. Maesaka, XM Marechal, T. Masuda, S. Matsubara, T. Matsumoto, T. Matsushita, S. Matsui, M. Nagasono, N. Nariyama, H. Ohashi, T. Ohata, T. Ohshima, S. Ono, Y. Otake, C. Saji, T. Sakurai, T. Sato, Kei Sawada, T. Seike, K. Shirasawa, T. Sugimoto, S. Suzuki, S. Takahashi, H. Takebe, K. Takeshita, K. Tamasaku, H. Tanaka, R. Tanaka, T. Tanaka, T. Togashi, K. Togawa, A. Tokuhisa, H. Tomizawa, K. Tono, S. Wu, M. Yabashi, M. Yamaga, A. Yamashita, K. Yanagida, C. Zhang, T. Shintake, H. Kitamura, and N. Kumagai, Nat. Photonics **6**, 540 (2012).
3. H.-S. Kang, C.-K. Min, H. Heo, C. Kim, H. Yang, G. Kim, I. Nam, S. Y. Baek, H.-J. Choi, G. Mun, B. R. Park, Y. J. Suh, D. C. Shin, J. Hu, J. Hong, S. Jung, S.-H. Kim, K. Kim, D. Na, S. S. Park, Y. J. Park, J.-H. Han, Y. G. Jung, S. H. Jeong, H. G. Lee, S. Lee, S. Lee, W.-W. Lee, B. Oh, H. S. Suh, Y. W. Parc, S.-J. Park, M. H. Kim, N.-S. Jung, Y.-C. Kim, M.-S. Lee, B.-H. Lee, C.-W. Sung, I.-S. Mok, J.-M. Yang, C.-S. Lee, H. Shin, J. H. Kim, Y. Kim, J. H. Lee, S.-Y. Park, J. Kim, J. Park, I. Eom, S. Rah, S. Kim, K. H. Nam, J. Park, J. Park, S. Kim, S. Kwon, S. H. Park, K. S. Kim, H. Hyun, S. N. Kim, S. Kim, S.-M. Hwang, M. J. Kim, C.-Y. Lim, C.-J. Yu, B.-S. Kim, T.-H. Kang, K.-W. Kim, S.-H. Kim, H.-S. Lee, H.-S. Lee, K.-H. Park, T.-Y. Koo, D.-E. Kim, and I. S. Ko, Nat. Photonics **11**, 708 (2017).
4. C. J. Milne, T. Schietinger, M. Aiba, A. Alarcon, J. Alex, A. Anghel, V. Arsov, C. Beard, P. Beaud, S. Bettoni, M. Bopp, H. Brands, M. Brönnimann, I. Brunnenkant, M. Calvi, A. Citterio, P. Craievich, M. Csatari Divall, M. Dällenbach, M. D'Amico, A. Dax, Y. Deng, A. Dietrich, R. Dinapoli, E. Divall, S. Dordevic, S. Ebner, C. Erny, H. Fitze, U. Flechsig, R. Follath, F. Frei, F. Gärtner, R. Ganter, T. Garvey, Z. Geng, I. Gorgisyan, C. Gough, A. Hauff, C. P. Hauri, N. Hiller, T. Humar, S. Hunziker, G. Ingold, R. Ischebeck, M. Janousch, P. Juranić, M. Jurcevic, M. Kaiser, B. Kalantari, R. Kalt, B. Keil, C. Kittel, G. Knopp, W. Koprek, H. T. Lemke, T. Lippuner, D. L. Sancho, F. Löhl, C. Lopez-Cuenca, F. Märki, F. Marcellini, G. Marinkovic, I. Martiel, R. Menzel, A. Mozzanica, K. Nass, G. L. Orlandi, C. O. Loch, E. Panepucci, M. Paraliev, B. Patterson, B. Pedrini, M. Pedrozzi, P. Pollet, C. Pradervand, E. Prat, P. Radi, J.-Y. Raguin, S. Redford, J. Rehanek, J. Réhault, S. Reiche, M. Ringele, J. Rittmann, L. Rivkin, A. Romann, M. Ruat, C. Ruder, L. Sala, L. Schebacher, T. Schilcher, V. Schlott, T. Schmidt, B. Schmitt, X. Shi, M. Stadler, L. Stingelin, W. Sturzenegger, J. Szlachetko, D. Thattil, D. M. Treyer, A. Trisorio, W. Tron, S. Vetter, C. Vicario, D. Voulot, M. Wang, T. Zamofing, C. Zellweger, R. Zennaro, E. Zimoch, R. Abela, L. Patthey, and H.-H. Braun, Appl. Sci. **7**, 720 (2017).
5. W. Decking, S. Abeghyan, P. Abramian, A. Abramsky, A. Aguirre, C. Albrecht, P. Alou, M. Altarelli, P. Altmann, K. Amyan, V. Anashin, E. Apostolov, K. Appel, D. Auguste, V. Ayvazyan, S. Baark, F. Babies, N. Baboi, P. Bak, V. Balandin, R. Baldinger, B. Baranasic, S. Barbanotti, O. Belikov, V. Belokurov, L. Belova, V. Belyakov, S. Berry, M. Bertucci, B. Beutner, A. Block, M. Blöcher, T. Böckmann, C. Bohm, M. Böhnert, V. Bondar, E. Bondarchuk, M. Bonezzi, P. Borowiec, C. Bösch, U. Bösenberg, A. Bosotti, R. Böspflug, M. Bousonville, E. Boyd, Y. Bozhko, A. Brand, J. Branlard, S. Briechle, F. Brinker, S. Brinker, R. Brinkmann, S. Brockhauser, O. Brovko, H. Brück, A. Brüdgam, L. Butkowski, T. Büttner, J. Calero, E. Castro-Carballo, G. Cattalanotto, J. Charrier, J. Chen, A. Cherepenko, V. Cheskidov, M. Chiodini, A. Chong, S. Choroba, M. Chorowski, D. Churanov,

https://doi.org/10.1017/hpl.2023.56 Published online by Cambridge University Press

W. Cichalewski, M. Clausen, M. Clement, C. Cloué, J. A. Cobos, N. Coppola, S. Cunis, K. Czuba, M. Czwalinna, B. D'Almagne, J. Dammann, H. Danared, A. de Zubiaurre Wagner, A. Delfs, T. Delfs, F. Dietrich, T. Dietrich, M. Dohlus, M. Dommach, A. Donat, X. Dong, N. Doynikov, M. Dressel, M. Duda, P. Duda, H. Eckoldt, W. Ehsan, J. Eidam, F. Eints, C. Engling, U. Englisch, A. Ermakov, K. Escherich, J. Eschke, E. Saldin, M. Faesing, A. Fallou, M. Felber, M. Fenner, B. Fernandes, J. M. Fernández, S. Feuker, K. Filippakopoulos, K. Floettmann, V. Fogel, M. Fontaine, A. Francés, I. Freijo Martin, W. Freund, T. Freyermuth, M. Friedland, L. Fröhlich, M. Fusetti, J. Fydrych, A. Gallas, O. García, L. Garcia-Tabares, G. Geloni, N. Gerasimova, C. Gerth, P. Geßler, V. Gharibyan, M. Gloor, J. Głowinkowski, A. Goessel, Z. Gołebiewski, N. Golubeva, W. Grabowski, W. Graeff, A. Grebentsov, M. Grecki, T. Grevsmuehl, M. Gross, U. Grosse-Wortmann, J. Grünert, S. Grunewald, P. Grzegory, G. Feng, H. Guler, G. Gusev, J. L. Gutierrez, L. Hagge, M. Hamberg, R. Hanneken, E. Harms, I. Hartl, A. Hauberg, S. Hauf, J. Hauschildt, J. Hauser, J. Havlicek, A. Hedqvist, N. Heidbrook, F. Hellberg, D. Henning, O. Hensler, T. Hermann, A. Hidvégi, M. Hierholzer, H. Hintz, F. Hoffmann, M. Hoffmann, M. Hoffmann, Y. Holler, M. Hüning, A. Ignatenko, M. Ilchen, A. Iluk, J. Iversen, J. Iversen, M. Izquierdo, L. Jachmann, N. Jardon, U. Jastrow, K. Jensch, J. Jensen, M. Jeabek, M. Jidda, H. Jin, N. Johansson, R. Jonas, W. Kaabi, D. Kaefer, R. Kammering, H. Kapitza, S. Karabekyan, S. Karstensen, K. Kasprzak, V. Katalev, D. Keese, B. Keil, M. Kholopov, M. Killenberger, B. Kitaev, Y. Klimchenko, R. Klos, L. Knebel, A. Koch, M. Koepke, S. Köhler, W. Köhler, N. Kohlstrunk, Z. Konopkova, A. Konstantinov, W. Kook, W. Koprek, M. Körfer, O. Korth, A. Kosarev, K. Kosiński, D. Kostin, Y. Kot, A. Kotarba, T. Kozak, V. Kozak, R. Kramert, M. Krasilnikov, A. Krasnov, B. Krause, L. Kravchuk, O. Krebs, R. Kretschmer, J. Kreutzkamp, O. Kröplin, K. Krzysik, G. Kube, H. Kuehn, N. Kujala, V. Kulikov, V. Kuzminych, D. La Civita, M. Lacroix, T. Lamb, A. Lancetov, M. Larsson, D. Le Pinvidic, S. Lederer, T. Lensch, D. Lenz, A. Leuschner, F. Levenhagen, Y. Li, J. Liebing, L. Lilje, T. Limberg, D. Lipka, B. List, J. Liu, S. Liu, B. Lorbeer, J. Lorkiewicz, H. H. Lu, F. Ludwig, K. Machau, W. Maciocha, C. Madec, C. Magueur, C. Maiano, I. Maksimova, K. Malcher, T. Maltezopoulos, E. Mamoshkina, B. Manschwetus, F. Marcellini, G. Marinkovic, T. Martinez, H. Martirosyan, W. Maschmann, M. Maslov, A. Matheisen, U. Mavric, J. Meißner, K. Meissner, M. Messerschmidt, N. Meyners, G. Michalski, P. Michelato, N. Mildner, M. Moe, F. Moglia, C. Mohr, S. Mohr, W. Möller, M. Mommerz, L. Monaco, C. Montiel, M. Moretti, I. Morozov, P. Morozov, D. Mross, J. Mueller, C. Müller, J. Müller, K. Müller, J. Munilla, A. Münnich, V. Muratov, O. Napoly, B. Näser, N. Nefedov, R. Neumann, R. Neumann, N. Ngada, D. Noelle, F. Obier, I. Okunev, J. A. Oliver, M. Omet, A. Oppelt, A. Ottmar, M. Oublaid, C. Pagani, R. Paparella, V. Paramonov, C. Peitzmann, J. Penning, A. Perus, F. Peters, B. Petersen, A. Petrov, I. Petrov, S. Pfeiffer, J. Pflüger, S. Philipp, Y. Pienaud, P. Pierini, S. Pivovarov, M. Planas, E. Pławski, M. Pohl, J. Polinski, V. Popov, S. Prat, J. Prenting, G. Priebe, H. Pryschelski, K. Przygoda, E. Pyata, B. Racky, A. Rathjen, W. Ratuschni, S. Regnaud-Campderros, K. Rehlich, D. Reschke, C. Robson, J. Roever, M. Roggli, J. Rothenburg, E. Rusiński, R. Rybaniec, H. Sahling, M. Salmani, L. Samoylova, D. Sanzone, F. Saretzki, O. Sawlanski, J. Schaffran, H. Schlarb, M. Schlösser, V. Schlott, C. Schmidt, F. Schmidt-Foehre, M. Schmitz, M. Schmökel, T. Schnautz, E. Schneidmiller, M. Scholz, B. Schöneburg, J. Schultze, C. Schulz, A. Schwarz, J. Sekutowicz, D. Sellmann, E. Semenov, S. Serkez, D. Sertore, N. Shehzad, P. Shemarykin, L. Shi, M. Sienkiewicz, D. Sikora, M. Sikorski, A. Silenzi, C. Simon, W. Singer, X. Singer, H. Sinn, K. Sinram, N. Skvorodnev, P. Smirnow, T. Sommer, A. Sorokin, M. Stadler, M. Steckel, B. Steffen, N. Steinhau-Kühl, F. Stephan, M. Stodulski, M. Stolper, A. Sulimov, R. Susen, J. Świerblewski, C. Sydlo, E. Syresin, V. Sytchev, J. Szuba, N. Tesch, J. Thie, A. Thiebault, K. Tiedtke, D. Tischhauser, J. Tolkiehn, S. Tomin, F. Tonisch, F. Toral, I. Torbin, A. Trapp, D. Treyer, G. Trowitzsch, T. Trublet, T. Tschentscher, F. Ullrich, M. Vannoni, P. Varela, G. Varghese, G. Vashchenko, M. Vasic, C. Vazquez-Velez, A. Verguet, S. Vilcins-Czvitkovits, R. Villanueva, B. Visentin, M. Viti, E. Vogel, E. Volobuev, R. Wagner, N. Walker, T. Wamsat, H. Weddig, G. Weichert, H. Weise, R. Wenndorf, M. Werner, R. Wichmann, C. Wiebers, M. Wiencek, T. Wilksen, I. Will, L. Winkelmann, M. Winkowski, K. Wittenburg, A. Witzig, P. Wlk, T. Wohlenberg, M. Wojciechowski, F. Wolff-Fabris, G. Wrochna, K. Wrona, M. Yakopov, B. Yang, F. Yang, M. Yurkov, I. Zagorodnov, P. Zalden, A. Zavadtsev, D. Zavadtsev, A. Zhirnov, A. Zhukov, V. Ziemann, A. Zolotov, N. Zolotukhina, F. Zummack, and D. Zybin, Nat. Photonics **14**, 391 (2020).

6. Z. Zhao, D. Wang, Z. Yang, and L. Yin, in *Proceedings of the 38th International Free Electron Laser Conference* (2018), paper MOP055.
7. J. Amann, W. Berg, V. D. Blank, F. J. Decker, Y. Ding, P. J. Emma, Y. Feng, J. C. Frisch, D. M. Fritz, J. B. Hastings, Z. Huang, J. Krzywiński, R. R. Lindberg, H. Loos, A. A. Lutman, H. D. Nuhn, D. Ratner, J. A. Rzepiela, D. Shu, Y. Shvyd'ko, S. Spampinati, S. Stoupin, S. Terentyev, E. M. Trakhtenberg, D. R. Walz, J. J. Welch, J. Wu, A. Zholents, and D. Zhu, Nat. Photonics **6**, 693 (2012).
8. K.-J. Kim, Y. Shvyd'ko, and S. Reiche, Phys. Rev. Lett. **100**, 244802 (2008).
9. R. R. Lindberg, K.-J. Kim, Y. Shvyd'ko, and W. M. Fawley, Phys. Rev. Spec. Top. Accel. Beams **14**, 010701 (2011).
10. C. Yang, K. Hu, Y. Zhu, X. Wang, Q. Li, Z. Xu, J. Wu, W. Zhang, Photonics **10**, 484 (2023).
11. W. Lu, B. Friedrich, T. Noll, K. Zhou, J. Hallmann, G. Ansaldi, T. Roth, S. Serkez, G. Geloni, A. Madsen, and S. Eisebitt, Rev. Sci. Instrum. **89**, 063121 (2018).
12. Y. Xu, C. Wu, J. Fan, Z. Wang, Y. Tong, Q. Huang, C. Yang, X. Dong, H. Jiang, and Z. Liu, Photonics **9**, 136 (2022).
13. A. K. Freund, G. Marot, H. Kawata, St. Joksch, E. Ziegler, L. E. Berman, and J. B. Hastings, Rev. Sci. Instrum. **63**, 442 (1992).
14. A. K. Freund, S. Joksch, H. Kawata, G. Marot, E. Ziegler, L. Berman, and J. Hastings, Rev. Sci. Instrum. **63**, 446 (1992).
15. V. Bushuev, Bull. Russian Acad. Sci. Phys. **77**, 12 (2013).
16. V. Bushuev, J. Surf. Investig. **10**, 1179 (2016).
17. B. Yang, S. Wang, and J. Wu, J. Synchrotron Rad. **25**, 166 (2018).
18. Z. Qu, Y. Ma, G. Zhou, and J. Wu, Opt. Express **28**, 30075 (2020).
19. Z. Qu, Y. Ma, G. Zhou, and J. Wu, Nucl. Inst. Methods Phys. Res. A **969**, 163936 (2020).
20. Z. Qu, Y. Ma, G. Zhou, and J. Wu, J. Synchrotron Rad. **27**, 1725 (2020).
21. Y. Shvyd'ko, *X-ray Optics – High-Energy-Resolution Applications* (Springer, 2004).
22. B. W. Batterman and H. Cole, Rev. Mod. Phys. **36**, 681 (1964).
23. A. Authier, *Dynamical Theory of X-ray Diffraction* (Oxford University, 2001).
24. A.-N. Jens and M. Des, *Elements of Modern X-ray Physics* (Wiley, 2011).
25. A. S. Okhotin, A. S. Pushkarskii, and V. V. Gorbachev, *Thermophysical Properties of Semiconductors* (Atom Publishing House, 1972).

https://doi.org/10.1017/hpl.2023.56 Published online by Cambridge University Press

26. K. G. Lyon, G. L. Salinger, C. A. Swenson, and G. K. White, J. Appl. Phys. **48**, 865 (1977).
27. O. Yasumasa and T. Yozo, J. Appl. Phys. **56**, 314 (1984).
28. M. Kazan, G. Guisbiers, S. Pereira, M. R. Correia, P. Masri, A. Bruyant, S. Volz, and P. Royer, J. Appl. Phys. **107**, 083503 (2010).
29. J.-S. Chung, "Darwin calculations of the Debye-Waller factor," PhD. Thesis (Purdue University, 1996).
30. R. Reeber and K. Wang, J. Electron. Mater. **25**, 63 (1996).
31. L. Wei, P. K. Kuo, R. L. Thomas, T. R. Anthony, and W. F. Banholzer, Phys. Rev. Lett. **70**, 3764 (1993).

https://doi.org/10.1017/hpl.2023.56 Published online by Cambridge University Press